



Analysis of Bright Source Hardness Ratios in the 4 yr Insight-HXMT Galactic Plane Scanning Survey Catalog

Chen Wang^{1,2} , Jin-Yuan Liao³ , Ju Guan³, Yuan Liu¹, Cheng-Kui Li³ , Na Sai^{4,5} , Jing Jin³ , and Shuang-Nan Zhang^{1,2,3} 

¹ Key Laboratory of Space Astronomy and Technology, National Astronomical Observatories, Chinese Academy of Sciences, Beijing 100101, China
cwang@bao.ac.cn

² University of Chinese Academy of Sciences, Beijing 100049, China

³ Key Laboratory of Particle Astrophysics, Institute of High Energy Physics, Chinese Academy of Sciences, Beijing 100049, China; liaojinyuan@ihep.ac.cn

⁴ Department of Astronomy, School of Physics and Technology, Wuhan University, Wuhan 430072, China

⁵ WHU-NAOC Joint Center for Astronomy, Wuhan University, Wuhan 430072, China

Received 2023 November 12; accepted 2023 December 22; published 2024 January 31

Abstract

We conduct a statistical analysis of the hardness ratio (HR) for bright sources in the 4 yr Galactic Plane Scanning Survey catalog of Insight-HXMT. Depending on the stable (variable) flux F_s (F_v) or spectrum S_s (S_v) of each source, the bright sources are classified into three groups: F_v & S_v , F_v & S_s , and F_s & S_s . Our study of the HR characteristics in different types of sources reveals that accretion-powered neutron star (NS) low-mass X-ray binaries (LMXBs) exhibit softer energy spectra than NS high-mass X-ray binaries (HMXBs), but harder energy spectra than black hole binaries in most cases. This difference is probably due to their different magnetic field strengths. Additionally, F_v & S_v LMXBs tend to be harder than F_v & S_s LMXBs below 7 keV, while the opposite is true for HMXBs. Our results suggest that LMXBs may dominate unclassified sources, and NS binaries are likely to be the primary type of X-ray binaries with ambiguous compact stars. By comparing the HR of transient sources in their outburst and low-flux states, it is found that the averaged HR of four sources in the two states are roughly comparable within uncertainties. We also investigate the spatial properties of the three groups and find that F_v & S_v sources are mainly located in the longitude of $-20^\circ < l < 9^\circ$, F_v & S_s sources cross the Galactic Plane, and F_s & S_s sources are predominantly concentrated in $19^\circ < l < 42^\circ$. In addition, analyzing the HR spatial distributions shows the absorption of soft X-rays (primarily below 2 keV) in the Galactic Plane.

Key words: catalogs – surveys – methods: data analysis – X-rays: general

1. Introduction

X-ray photons can be generated through a variety of physical processes, such as the thermal processes dominated by bremsstrahlung in accreting white dwarf systems (e.g., Mukai 2017), the inverse Compton scattering in hot corona of black hole (BH) binaries (e.g., Zhang 2013), blackbody radiation emitted from neutron star (NS) surfaces (e.g., Mitsuda et al. 1984), and synchrotron radiation from jets in accreting binary systems (e.g., Russell & Fender 2008). The diverse mechanisms produce characteristic X-ray spectra, including power-law, blackbody, and thermal bremsstrahlung, etc. Soft X-rays are typically produced by thermal radiation, while hard X-rays are related to non-thermal processes. Therefore, studying the radiation in different energy ranges is crucial for understanding the radiation mechanisms and physical processes in X-ray sources.

The hardness ratio (HR) is a relative measurement between high-energy and low-energy X-ray fluxes and calculated by comparing count rates of the two energy bands (Jin et al. 2006). It is a widely utilized essential tool to investigate the spectral

properties and radiation mechanisms of X-ray sources. For example, the HR can distinguish between different classes of objects based on their unique spectral shapes and variability patterns. In exploring properties of compact systems, the HR is particularly useful in analyzing Hardness–Intensity Diagram (HID), from which information of X-ray energy spectra and a more comprehensive evolutionary picture can be presented (Remillard & McClintock 2006; Zhang 2013). Additionally, the HR can provide information of state transitions which can reflect how the energy is released in the accretion disks near BHs and NSs (Zhang et al. 1997).

The HR analysis has a positive impact on reflecting the nature of the energy spectra and understanding the physical processes behind the radiation. Its calculations and analyses are crucial aspects in scanning or slew X-ray surveys (see e.g., Voges et al. 1999; Cusumano et al. 2010; Boller et al. 2016; Hong et al. 2016; Kawamuro et al. 2018). The HR has been used to discuss the overall properties of different types of sources, predict the possible types of unidentified sources (Hori et al. 2018), search for counterparts of detected sources

Table 1
Payloads of Insight-HXMT

Payloads	Geometrical Area (cm ²)	Detector Materials	Small FOV (FWHM)	Large FOV (FWHM)	Energy Band1 ^a (keV)	Energy Band2 ^b (keV)
HE	5100	NaI(Tl)/CsI(Na)	1°1 × 5°7	5°7 × 5°7	20–250	25–100
ME	952	Si-PIN	1° × 4°	4° × 4°	5–40	7–40
LE	384	SCD ^c	1°6 × 6°	4° × 6°	0.7–13	1–7

Notes.

^a The energy bands that three instruments covered.

^b The energy bands that are used in Insight-HXMT GPSS.

^c Swept Charge Device.

(Bahramian et al. 2021), analyze the spectral characteristics of different type of sources (Krivonos et al. 2015), and characterize the distribution regularities in various spatial regions (Saxton et al. 2008). However, most previous HR analyses in X-ray surveys did not distinguish between sources with stable and variable spectrum/flux.

Insight-HXMT is a collimation modulated telescope with large field of views (FOVs) and a wide energy band (1–250 keV). It carries three scientific payloads: the High Energy X-ray Telescope (HE), the Medium Energy X-ray Telescope (ME), and the Low Energy X-ray Telescope (LE). Their parameters are listed in Table 1, and a detailed introduction can be found in Zhang et al. (2020). Galactic Plane Scanning Survey (GPSS) is one of its core scientific objectives, occupying 1/3 of its total annual observational time. More than 1300 X-ray sources have been monitored at 1–100 keV after its 4 yr commission (Wang et al. 2023). Thanks to the wide band coverage, the HR of the monitored sources can be calculated and analyzed for various combinations of energy bands. Wang et al. (2023) has presented a preliminary summary of the characteristics of the HR of low-mass X-ray binaries (LMXBs) and high-mass X-ray binaries (HMXBs). In this work, we focus on a more detailed analysis of the HR of bright sources in the Insight-HXMT GPSS catalog to provide a more comprehensive understanding of the spectral properties of the monitored sources.

The data and reduction procedures are described in Section 2. The result and discussion are presented in Section 3. The summary is drawn in Section 4.

2. Data and Reduction

The GPSS data reduction and catalog have been presented in detail in Sai et al. (2020) and Wang et al. (2023); here we only make a brief overview. The Insight-HXMT GPSS utilizes various energy bands, including 1–2, 2–4, 4–6, 2–6, 3–5, 5–7, 7–40 and 25–100 keV. This work is primarily focused on the energy bands above 2 keV, and only includes data obtained before 2020 August for the 1–2 keV because the data accuracy at 1–2 keV has degraded due to aging of LE. During each observation, the FOVs cross various sources, whose fluxes and

positions can be reconstructed via point-spread function (PSF) fitting (Nang et al. 2020). Long-term light curves at various energy bands are obtained after a survey period. The published Insight-HXMT GPSS catalog, from 2017 June to 2021 August, contains information on over the 1300 monitored sources.

The HR of each source that is bright both in the hard and soft bands is calculated. The criteria to identify a bright source is that it is positively detected with a signal-to-noise ratio (S/N) greater than 5. The averaged flux and S/N are calculated as follows:

$$\bar{f} = \frac{\sum_i \omega_i f_i}{\sum_i \omega_i}, \quad (1)$$

$$\omega_i = \frac{1}{\sigma_i^2}, \quad (2)$$

$$\sigma^2(\bar{f}) = \frac{1}{(\sum_i \omega_i)^2} \sum_i \omega_i^2 \sigma_i^2 = \frac{1}{\sum_i \frac{1}{\sigma_i^2}}, \quad (3)$$

and

$$\overline{S/N} = \frac{\bar{f}}{\bar{\sigma}}, \quad (4)$$

where f_i and σ_i represent the best-fitting flux of a source in the i th observation and the corresponding 1σ error. Under the Gaussian distribution, the HR and its corresponding error are traditionally defined and derived as follows:

$$\text{HR} = \frac{H}{S}, \quad (5)$$

and

$$\sigma_{\text{HR,stat}} = \frac{H}{S} \sqrt{\frac{\sigma_{S,\text{stat}}^2}{S^2} + \frac{\sigma_{H,\text{stat}}^2}{H^2}}, \quad (6)$$

where H and S are the count rates of the hard and soft energy bands, respectively. $\sigma_{H,\text{stat}}$ and $\sigma_{S,\text{stat}}$ are the statistical errors of fluxes at the hard and soft bands, respectively. However, the HR definition may be problematic in cases of Poisson distribution with low counts. Jin et al. (2006) proposed an alternative derivation of $\text{HR} = \frac{H}{S+2}$ (or $\text{HR} = \frac{H-1/2}{S+3/2}$), which statistically robust. It was found that the confidence from the

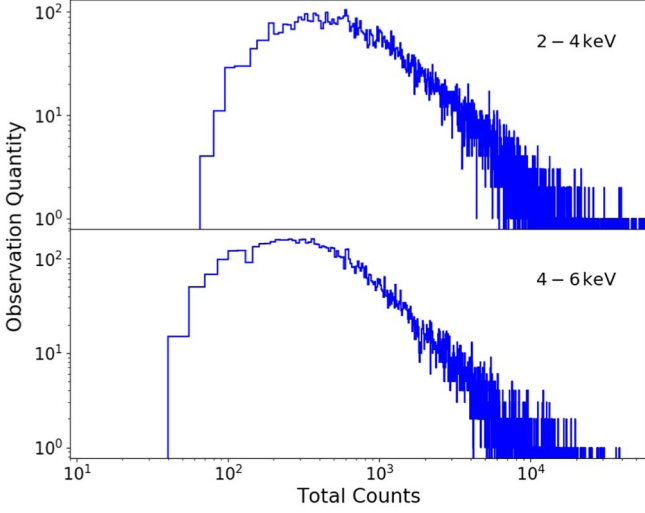


Figure 1. The histogram (bin size = 15) of the observation quantity with varying total counts in each observation.

traditional and their methods coincides when the number of counts reaches 15 and above. In the catalog of Insight-HXMT, some sources have low count rates, whereas their total counts for each observation exceed a few tens. Therefore, Equations (5) and (6) are reliable for the HR calculations in our work. The top and bottom panels in Figure 1 illustrate the distribution of total counts for all bright sources at 2–4 and 4–6 keV, respectively. It is evident that the total counts in both bands are significantly higher than 15.

Consequently, the long-term HR can be obtained for various combinations of hard and soft bands. Furthermore, the averaged HR and the corresponding S/N are calculated based on Equations (1)–(4), in which f_i and σ_i are replaced with the i th HR and its associated error. Only the sources with an averaged S/N of HR greater than 3 are utilized in the subsequent statistical analysis.

The Crab Nebula (hereafter the Crab) is known for its stable flux and spectrum, making it a commonly used calibration source (e.g., Sugizaki et al. 2011; Madsen et al. 2015). The fluctuation observed in its long-term light curve is considered to be instrumental systematic error. Accordingly, the systematic errors of the HR at related energy bands are calculated based on the corresponding long-term HR of the Crab. The systematic errors can be achieved by solving the following equations:

$$\sum_i^N \frac{(x_i - \bar{x})^2}{\sigma_{\text{total},i}^2} = N - 1, \quad (7)$$

$$\sigma_{\text{total},i}^2 = \sigma_{\text{sys}}^2 + \sigma_{\text{stat},i}^2, \quad (8)$$

$$\omega_i = \frac{1}{\sigma_{\text{total},i}^2}, \quad (9)$$

and

$$\bar{x} = \frac{\sum_i \omega_i x_i}{\sum_i \omega_i}, \quad (10)$$

where N is the number of data points, x_i and $\sigma_{\text{total},i}$ are the i th HR and the corresponding total error of the Crab, $\sigma_{\text{stat},i}$ and σ_{sys} are the statistical and systematic errors, respectively. \bar{x} is the average HR. The systematic errors of the HR for various combinations of hard and soft bands are listed in Table 2.

Three examples are illustrated in Figure 2, where each panel from top to bottom shows the long-term light curves at 2–4, 4–6 keV, and the long-term HR (4–6 keV/2–4 keV). It can be seen that the fluxes and HR of the Crab are generally stable as expected. The fluxes of Cen X–3 show strong variations, while its HR slightly varies. In comparison, both the flux and HR of Cyg X–1 vary dramatically. Therefore, it is crucial to quantify the flux and HR variability of each source, which is a significant aspect of this work.

The excess variance (F_{rms}) is a practical tool for quantifying flux variability (Vaughan et al. 2003; Hori et al. 2018), and can be calculated using the equations:

$$S^2 = \frac{1}{N-1} \sum_i^N (f_i - \bar{f})^2, \quad (11)$$

$$F_{\text{rms}} = \frac{S^2 - \bar{\sigma}^2}{\bar{f}^2}, \quad (12)$$

and

$$d F_{\text{rms}} = \sqrt{\left(\sqrt{\frac{2}{N}} \times \frac{\bar{\sigma}^2}{\bar{f}^2} \right)^2 + \left(\sqrt{\frac{\bar{\sigma}^2}{N}} \times \frac{2\sqrt{F_{\text{rms}}}}{\bar{f}} \right)^2}, \quad (13)$$

where N is the number of data points on a long-term light curve, f_i is the i th flux, $\bar{\sigma}^2$ is the mean of the square of the statistical error. A source is considered to be flux-variable (F_v) if $F_{\text{rms}} - d F_{\text{rms}} > F_{\text{rms}}^{\text{Crab}}$; otherwise, it is a flux-stable (F_s) source. The values of F_{rms} of Cen X–3 and Cyg X–1 are listed in columns (2) and (3) of Table 3, which are larger than $F_{\text{rms}}^{\text{Crab}}$ at both 2–4 and 4–6 keV bands. Therefore, Cen X–3 and Cyg X–1 are flux-variable sources at the two energy bands.

A source is considered to be spectrum-stable (S_s) if it has a stable energy spectral shape at both analyzed hard and soft bands. Quantitatively, the fluctuation of the long-term HR of this kind of sources does not exceed the corresponding systematic error. To quantify the variations in the HR, a standard χ^2 test (Wani & Gaur 2020) is employed as follows

$$\chi^2 = \sum_i^N \frac{(x_i - \bar{x})^2}{\sigma_{\text{total},i}^2}, \quad (14)$$

where x_i and $\sigma_{\text{total},i}$ are the same as those in Equation (7). Therefore, a source is spectrum-variable (S_v) if $\chi^2 > \chi_{\text{limit},\nu}^2$; otherwise, it is a spectrum-stable (S_s) one. The significance

Table 2
The Number of Sources with Different Flux and Spectral Variability in Various Combinations of Hard and Soft Bands

<i>H</i> Band ^a (keV)	S ^b :1–2 keV				S:2–4 keV				S:3–5 keV				S:5–7 keV				S:2–6 keV			
	σ_{sys}	$F_v \& S_v$	$F_v \& S_s$	$F_s \& S_s$	σ_{sys}	$F_v \& S_v$	$F_v \& S_s$	$F_s \& S_s$	σ_{sys}	$F_v \& S_v$	$F_v \& S_s$	$F_s \& S_s$	σ_{sys}	$F_v \& S_v$	$F_v \& S_s$	$F_s \& S_s$	σ_{sys}	$F_v \& S_v$	$F_v \& S_s$	$F_s \& S_s$
2–4	0.45	57	25	54
4–6	0.78	45	35	48	1.02	63	49	61
5–7	2.0	40	34	49	2.18	54	45	49	1.53	45	56	70
7–40	2.91	31	3	2	3.20	36	8	2	2.71	38	7	2	3.52	35	11	1	3.11	38	8	2
25–100	2.07	16	9	3	2.39	30	6	4	2.51	28	8	2	3.01	23	11	2	2.49	30	7	4

Notes.

^a This column represents the hard energy bands: 2–4, 4–6, 5–7, 7–40 and 25–100 keV.

^b “S” represents the soft energy band.

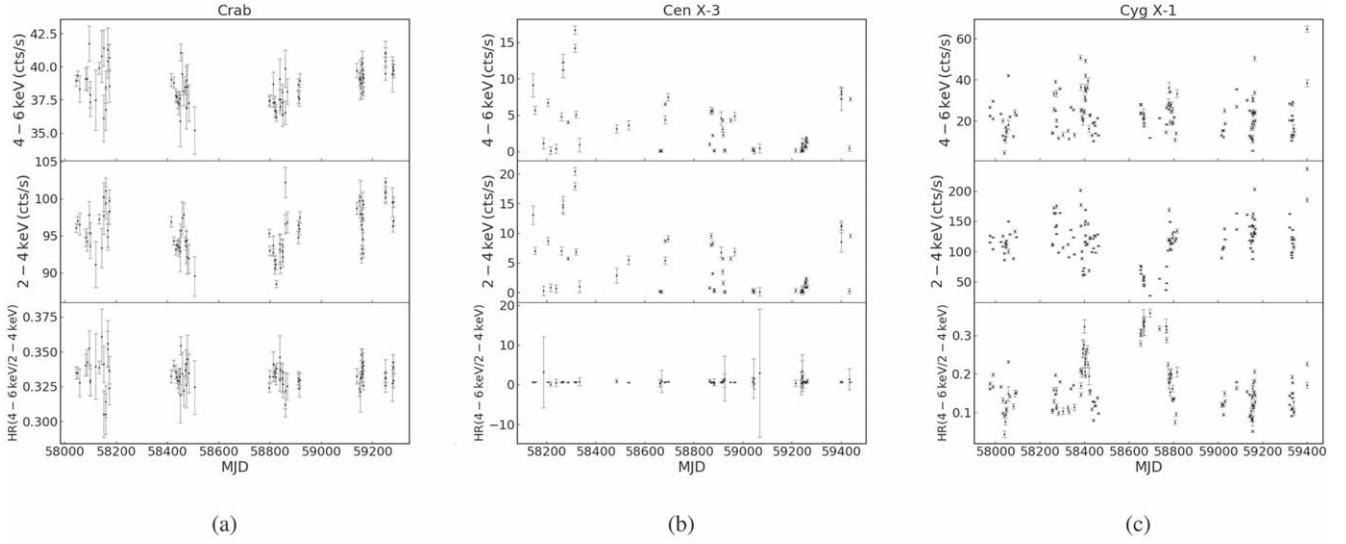


Figure 2. The long-term light curves and HR of Crab, Cen X–3, and Cyg X–1, respectively.

Table 3
The Variation of Flux and HR

Source Name	$F_{\text{rms}}^{2-4 \text{ keV}}$	$F_{\text{rms}}^{4-6 \text{ keV}}$	DoF	$\chi_{0.5, \nu}^2$	χ^2
Crab	0.001 ± 0.0001	0.0007 ± 0.0002	78	77.33	77.30
Cen X–3	0.137 ± 0.001	0.271 ± 0.004	64	63.33	38.34
Cyg X–1	9.2 ± 0.2	10.8 ± 0.3	146	145.33	17808.55

level corresponding to the χ^2 of Crab is denoted as “limit,” and ν denotes the degrees of freedom (DoF). In Figure 2(a), $\chi_{\nu}^2 = 77.3$ for Crab ($\nu = 78$), corresponding to a significance level of 0.5. Thus, $\chi_{0.5, \nu}^2$ is used to determine the variability of the HR (4–6 keV/2–4 keV). The $\chi_{0.5, \nu}^2$ and χ^2 of Cen X–3 and Cyg X–1 are listed in column (5) of Table 3. It is evident that the χ^2 of Cen X–3 is less than $\chi_{0.5, 64}^2$, and the χ^2 of Cyg X–1 is far larger than $\chi_{0.5, 146}^2$. As expected, Cen X–3 is spectrum-stable, but Cyg X–1 is not.

In general, sources that exhibit flux stability are typically spectrum-stable, while flux-variable sources may be either spectrum-stable or spectrum-variable. Consequently, the monitored sources can be divided into three groups: (1) flux- and spectrum-variable ($F_v \& S_v$), (2) flux-variable but spectrum-stable ($F_v \& S_s$), and (3) flux- and spectrum-stable ($F_s \& S_s$). The number of bright sources with different combinations of hard and soft bands can be found in Table 2. The machine readable file records all the details of source names, the HR (and error) with different combinations of hard and soft bands, χ^2 of long-term HR, spectral variability, F_{rms} (and error), and flux variability for all bright sources detected. All statistical analysis data in this work can be found in this file, with some of the content relating to LMXB and HMXB extracted in Table A1 and Table A2 in Appendix A.

3. Result and Discussion

The values of HR for the bright sources listed in the Insight-HXMT 4 yr GPSS catalog across various combinations of hard and soft bands are derived. In this work, the averaged HR of each source is adopted. This section encompasses a series of statistical analyses, including an examination of the relationship between HR and source types, an investigation into the spatial distributions for the sources belonging to the three variability groups, and an analysis of the correlation between HR and spatial distributions, respectively.

3.1. General HR Properties of X-Ray Binaries

Bright X-ray sources on the Galactic plane are predominantly accretion-powered X-ray binaries (XRBs), which is also evident in the Insight-HXMT catalog. Thus, in this section, our focus is on analyzing the overall HR characteristics of XRBs. These binary systems can be classified into LMXBs and HMXBs based on the mass of the donor star or into NS binaries and BH binaries based on the primary object. NS binaries exhibit brightness variations on various timescales (Reig 2011), while most BH binaries are transient systems (Remillard & McClintock 2006). Therefore, fluxes of most XRBs are expected to be variable. Moreover, their spectra exhibit different shapes because X-rays in accreting systems emit

from specific regions due to their different magnetic fields and with/without a solid surface:

1. In a highly magnetized NS system ($B \sim 10^{12}$ G), the accretion flow is guided and funneled onto the poles, which forms accretion columns (White et al. 1983; Bildsten et al. 1997). Within the columns, radiation processes, such as bremsstrahlung, cyclotron and black-body emissions, can occur due to the high radiation pressure, temperature, and strong magnetic field. These processes result in the emission of bright X-rays (Becker & Wolff 2007).
2. In the NS systems with weak magnetic fields, the tunneling effect is not so effective that a Keplerian disk is formed instead (Alpar et al. 1982). Most of the accreting gas is pulled into the circular orbit and gradually transferred to the surface of the primary star (Mitsuda et al. 1984; Lamb & Boutloukos 2008). Consequently, the X-ray generally consists of soft components (below a few keV), which are expected to come from thermal emission from the accretion disk and NS surface (Poutanen 2006).
3. Compared to NS systems, the primary star in a BH system is typically thought to lack strong macroscopic magnetic fields and a solid surface (Zhang 2013). In expectation, BH binaries spend most of their lives in a quiescent state, during which the X-ray luminosity is very low, and the radiation is mainly generated by thermal emission from the accretion disk (McClintock & Remillard 2006). However, during their outburst periods, they exhibit various states, including hard state, thermal state, and steep power state, each with dominant X-rays originating from different regions such as disk, jet, or corona (Remillard & McClintock 2006).

It can be concluded that the X-ray spectral hardness of accreting NS binaries with strong magnetic fields are harder than those with weak magnetic fields. This is supported by, for example, Hoshi (1984). In contrast, the spectral hardness of BH systems is closely related to different states. When the proportion of non-thermal radiation from the corona is small, their energy spectra are expected to be softer than those of NS binaries.

Then we conduct a comparison of the HR characteristics of LMXBs and HMXBs separately.⁶ To investigate whether there are any systematic changes as the energy of the hard band increases, the soft band is fixed at 2–4 keV, and the hard band is sequentially selected as 4–6, 5–7, 7–40, and 25–100 keV. The median values⁷ of the HR are utilized to quantify the

⁶ We classify the XRBs into LMXBs and HMXBs here for the reason that the types of some primary stars are unclear.

⁷ In this paper, the median value of HR refers to the middle value of HR if data count is odd; otherwise the weighted average of the middle two values of HRs.

overall changes. The distributions of the number of sources with HR greater than a given value for different combinations of hard and soft bands are shown in Figure 3, where panels (a) to (d) represent all sources, $F_v \& S_v$, $F_v \& S_s$, and $F_s \& S_s$ sources, respectively. Each color corresponds to a different hard band, and the vertical lines indicate the location of the median values. Table 4 lists the numbers of LMXBs and HMXBs in different variability groups, while Table 5 lists the corresponding median values. Based on Figure 3 and Tables 4 and 5, the following conclusions can be drawn:

1. As expected, LMXBs and HMXBs with stable fluxes constitute a small proportion.
2. The energy spectra of HMXBs tend to be harder than those of LMXBs overall, regardless of the selection of the hard band. This trend is observed in all sources, $F_v \& S_v$, and $F_v \& S_s$ sources.
3. In LMXBs, the energy spectra of $F_v \& S_v$ sources tend to be harder compared to the $F_v \& S_s$ sources below 7 keV. However, in HMXBs, the opposite trend is observed.

That the HR of HMXBs is consistently higher than that of LMXBs is in line with Fabbiano (2006) and consistent with the former description:

1. Young NS HMXBs usually retain most of their initial high magnetic field ($B \sim 10^{12}$ G) strengths due to their relatively short accretion time (Psaltis 2004).
2. The magnetic fields of LMXBs are generally weak and range from 10^{11} G down to 10^7 G or even less (Lamb & Boutloukos 2008), because the LMXBs are usually very old and the prolonged accretion weakens the magnetic fields of the NSs (Psaltis 2004).
3. Since NS binaries are believed to be significantly more abundant than BH binaries (Belczynski & Ziolkowski 2009), the influence of BH binaries on the results is insignificant.

3.2. HR Distributions of Different Types of Bright X-Ray Sources at 2–7 keV

In the 4 yr catalog of Insight-HXMT, bright sources are primarily detected below 7 keV. Therefore, we investigate the HR characteristics of the sources in the 2–7 keV bands to identify any characteristics and deduce possible classifications for the unclassified sources. Of the 142 X-ray bright sources in the 2–4, 4–6, 3–5, and 5–7 keV band, seven are excluded for statistical analysis due to the very small sample size of each type. These sources include one cluster of galaxies (Oph Cluter), two Cataclysmic Binaries (IGR J18308–1232, SS Cyg), one double or multiple star system (AX J1847.6–0156), one radio source (AX J1841.3–0455), one Seyfert 2 galaxy (IGR J16024–6107), and one Be star (gam Cas). Out of the remaining 135 sources, they mainly fall into five categories:

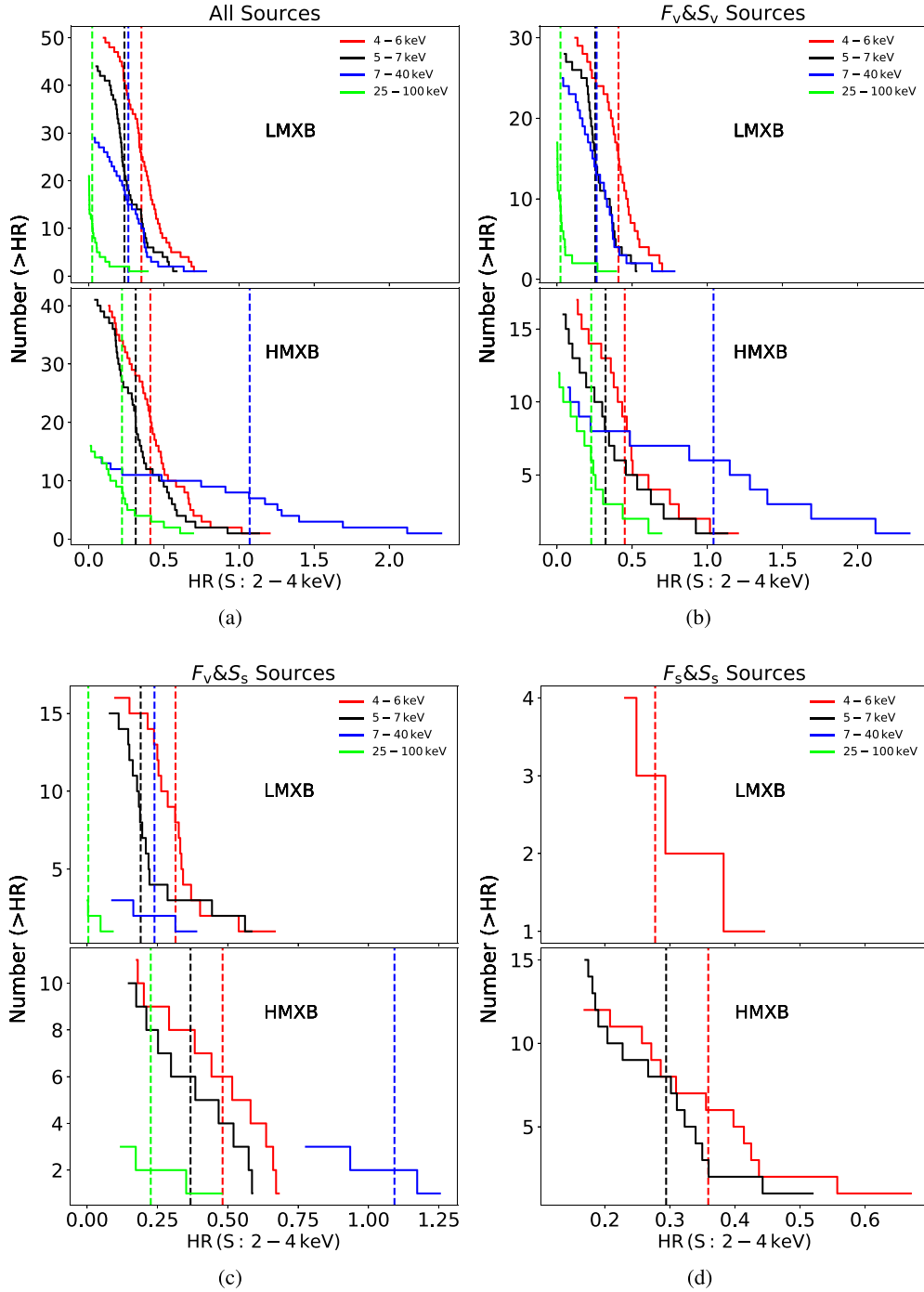


Figure 3. The relations between the cumulative numbers and HR; X-axis is HR, and Y-axis is the number of sources with HR higher than the value corresponding to X-axis. The dashed lines are the median values of HR.

LMXBs, HMXBs, pulsars, supernova remnants (SNRs), and Seyfert 1 galaxies, along with several unclassified sources. The LMXBs and HMXBs are further classified into NS and BH binaries, while seven have unknown primary objects. Their values of HR are calculated at two combinations of hard and

soft bands: 5–7 keV/3–5 keV (hereafter “HR1”) and 4–6 keV/2–4 keV (hereafter “HR2”). Figure 4 displays the distribution of the 135 sources between “HR1” and “HR2,” with each type assigned a distinct color. To quantify the correlations between “HR1” and “HR2” of different sources

Table 4
The Source Number of LMXBs and HMXBs (S: 2–4 keV)

<i>H</i> Band	LMXB All	LMXB $F_v \& S_v$	LMXB $F_v \& S_s$	LMXB $F_s \& S_s$	HMXB All	HMXB $F_v \& S_v$	HMXB $F_v \& S_s$	HMXB $F_s \& S_s$
4–6 keV	50	30	16	4	40	17	11	12
5–7 keV	44	28	15	1	41	16	10	15
7–40 keV	29	25	3	1	14	11	3	0
25–100 keV	21	17	3	1	16	12	3	1

Table 5
The Median Values of HR (S: 2–4 keV)

<i>H</i> Band	LMXB All	LMXB $F_v \& S_v$	LMXB $F_v \& S_s$	LMXB $F_s \& S_s$	HMXB All	HMXB $F_v \& S_v$	HMXB $F_v \& S_s$	HMXB $F_s \& S_s$
4–6 keV	0.350 ± 0.003	0.409 ± 0.003	0.314 ± 0.004	0.28 ± 0.03	0.41 ± 0.05	0.45 ± 0.01	0.48 ± 0.05	0.36 ± 0.04
5–7 keV	0.24 ± 0.05	0.254 ± 0.002	0.190 ± 0.005	0.35 ± 0.10	0.31 ± 0.08	0.323 ± 0.002	0.37 ± 0.02	0.29 ± 0.06
7–40 keV	0.263 ± 0.001	0.263 ± 0.001	0.24 ± 0.02	0.367 ± 0.04	1.0 ± 0.1	1.041 ± 0.004	1.1 ± 0.1	...
25–100 keV	0.023 ± 0.002	0.023 ± 0.002	0.0045 ± 0.0007	0.13 ± 0.03	0.22 ± 0.03	0.23 ± 0.02	0.23 ± 0.07	0.14 ± 0.02

shown in this figure, the correlation coefficients ($\rho_{X,Y} = \frac{\text{cov}(X,Y)}{\sigma_X \sigma_Y}$) are calculated. Noting that, the correlation coefficients between HR1 and HR2 have limited physical significance and are calculated to quantify potential differences across different source types. For LMXBs, HMXBs, Pulsars, SNRs, Seyfert1 galaxies, and unclassified sources, the correlation coefficients are determined to be 0.62, 0.93, 0.66, 0.69, 0.48, and 0.59, respectively. In Figure 5, the distribution of different primary stars in LMXBs and HMXBs is depicted, with the unknown object represented as “?”. The corresponding histograms are presented in Figures 6 and 7.

From Figures 4 and 6, it can be seen that:

1. When the hard and soft bands are selected as 5–7 and 3–5 keV (“HR1”), the values of HR of LMXBs are mainly concentrated between 0.2 and 0.6. However, when considering the “HR2” values, they tend to cluster around 0.4.
2. The median HR of HMXBs is the highest among the five types.
3. Compared to HMXBs and LMXBs, the distribution range of pulsars, SNRs, and Seyfert 1 galaxies is narrower, and their values of HR tend to be lower in “HR2” than in “HR1.”
4. The correlation coefficient and overall distribution of the unclassified sources are more similar to that of LMXBs. Although the unclassified sources may contain various types of sources, LMXBs are likely to account for a higher percentage compared to others.

Figures 5 and 7 clearly show that the energy spectra of NS binaries are generally harder than those of BH binaries, as is indicated by both “HR1” and “HR2.” Furthermore, the spectra

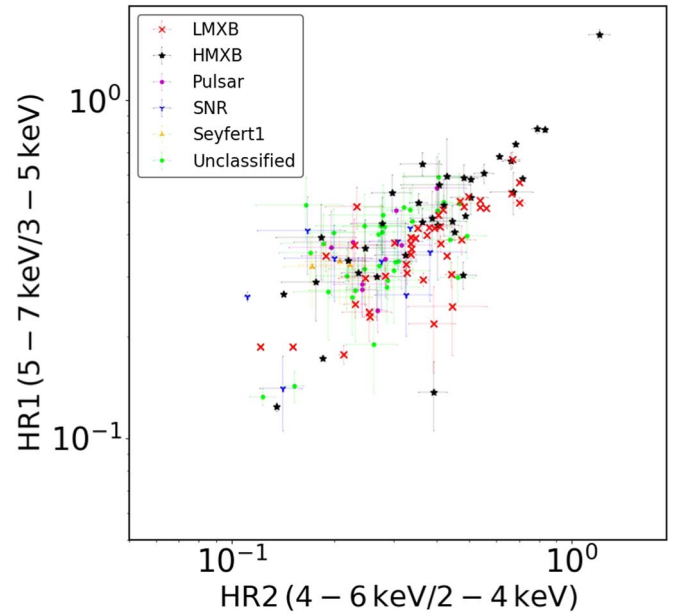


Figure 4. The distributions of “HR1” and “HR2” for 135 sources. Different colors are assigned to different source types.

of NS LMXBs are generally softer than those of NS HMXBs. They are consistent with and further confirmed the results presented in Section 3.1.

Based on the HR distributions, one LMXB and six HMXBs with unclear primary types can be speculated upon the followings:

1. The proportion of the NS and BH binaries in the region where the HR of “?” are located can be used to predicate their compact types.

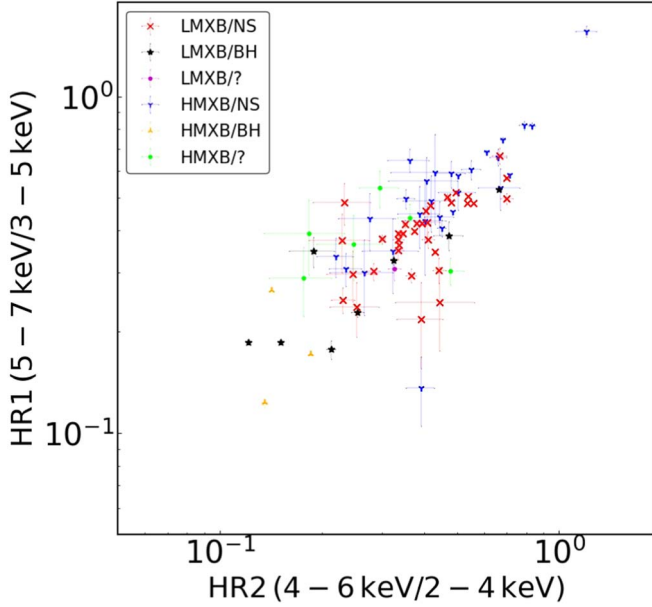


Figure 5. The distributions of “HR1” and “HR2” for XRBs. Different colors are assigned to different source types.

2. The overall change trend of the HR of “?” from “HR1” to “HR2” can be used to speculate their compact types, as it tends to be closer to the HR trend of either NS or BH binaries.

In Figure 7, the location of “LMXB/?” is dominated by NS LMXBs, indicating that the unknown compact object is likely to be an NS. Similarly, the six unknown compact objects in HMXBs may also be predominantly NS binaries, as their overall HR trend is closer to that of NS binaries.

3.3. The HR between Low-flux and Outburst States of Transient XRBs

After the first 4 yr of the Insight-HXMT GPSS, the outburst outbursts⁸ of seven transient XRBs (GX 339–4, MAXI J1820+070, MAXI J1348+630, 4U 1722–30, GRS 1915+105, SWIFT J0243.6+6124, and 1A 0535+262, labeled as # “1” to “7” in Figure 8, respectively) are monitored. Their long-term light curves and HR are illustrated in Figure B1 of Appendix B. The outburst and low-flux states are distinguished based on the relationship between the 3σ lower limit of flux and the sensitivity. In this section, their averaged HR (5–7 keV/3–5 keV) of the two states are compared, as shown in Figure 8. Table 6 lists their locations, source types, and averaged HR of the two states. It can be seen that:

1. Although the averaged HR of GX 339–4, MAXI J1820+070, and MAXI J1348–630 (# “1,” “2” and “3”) have larger uncertainties in the low-flux states, it is evident that their averaged HR are larger than those in their outburst states. This is consistent with the q-shaped track in the HID diagram, which is commonly used to describe the global evolution of BH transients (Homan & Belloni 2005).
2. During the observed low-flux and outburst states of 4U 1722–30, GRS 1915+105, SWIFT J0243.6+6124 and 1A 0535+262 (# “4” to “7”), their averaged HR in low-flux state have smaller uncertainties and are closer to that in their outburst states.
3. The HR of the two NS HMXBs (# “6” and “7”) are consistently larger than those of LMXBs and BH HMXBs, both in the low-flux and outburst states. The result agrees with the conclusion in Section 3.1.

3.4. HR Distribution Characteristics of Bright Source at 2–100 keV

A total of 31 bright sources are detected across the energy bands of 2–6, 7–40, and 25–100 keV, comprising of one SNR, 18 LMXBs, and 12 HMXBs. The spectrum of each source is roughly simplified as an absorbed power-law model, with the interstellar absorption (N_{H}) obtained from the NASA website.⁹ The photon index (Γ) and normalization (N_0) are obtained via the following steps:

1. A series of power-law models with a unit N_0 and varying Γ (ranging from –2 to 8) are used to convolve with the response matrices at 2–6, 7–40, and 25–100 keV. This provides us a series of predicted fluxes at the three energy bands for different Γ .
2. To obtain N_0 corresponding to each Γ , we divide the 4 yr averaged flux at one energy band by the series of predicted fluxes at the same band.
3. To obtain the theoretical detected counts at the three energy bands that correspond to different power-law spectra, all predicted fluxes are multiplied by their corresponding N_0 .
4. The processed fluxes are then compared to the 4 yr averaged fluxes at the three energy bands. The model that corresponds to the optimal chi-squared value is considered as the source model.

The final results are presented in Table 7. It is important to note that the listed models are based on rough calculations using averaged fluxes, and are intended to estimate the overall energy spectrum characteristics of XRBs. However, since most listed XRBs are spectrally variable sources, the true spectral shapes are likely more complex than

⁸ The peak flux recorded by Insight-HXMT GPSS is more than two orders of magnitude larger than the sensitivity limit.

⁹ <https://heasarc.gsfc.nasa.gov/cgi-bin/Tools/w3nh/w3nh.pl>

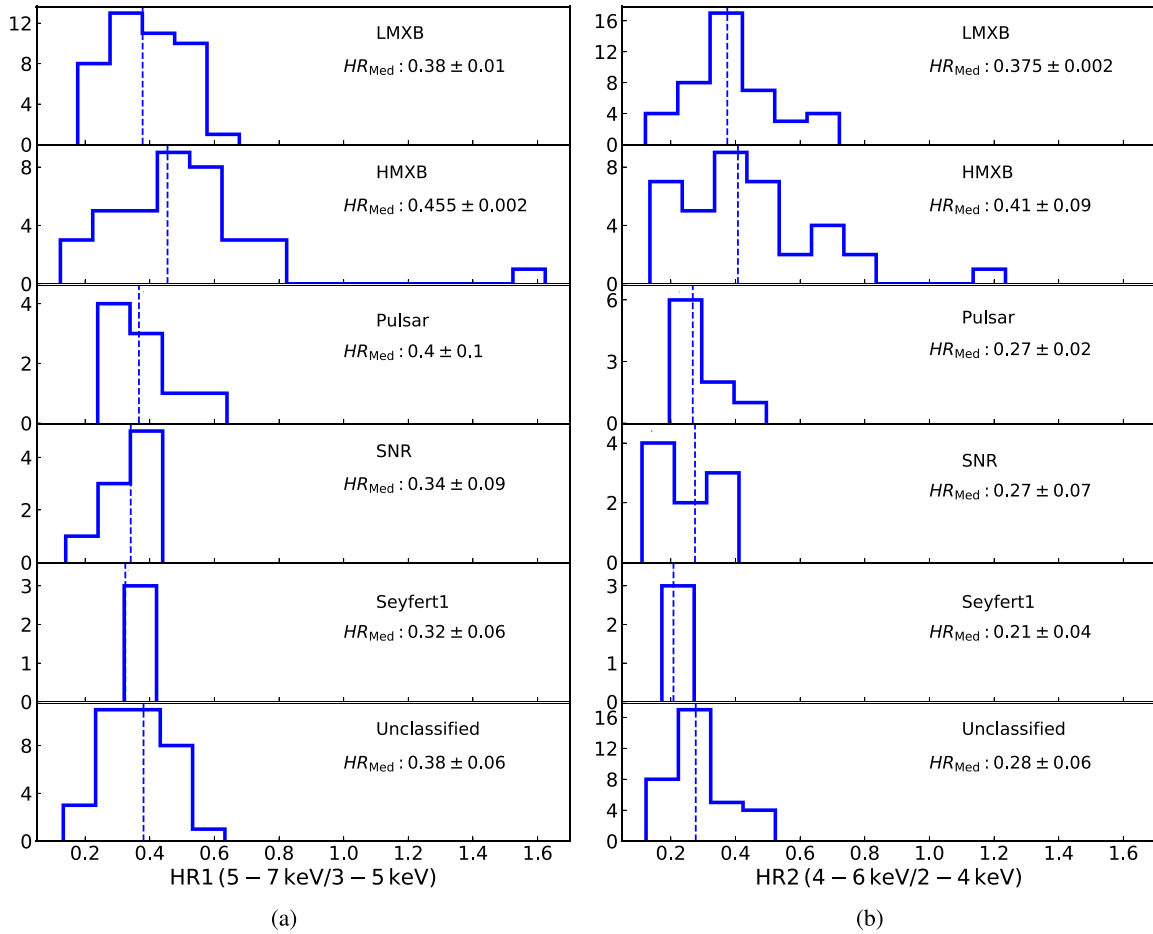


Figure 6. The histogram (bin size = 0.1) of HR distribution for the 135 bright X-ray sources. The y-axis represents the source number, and the x-axis corresponds to HR. Additionally, the dashed lines indicate the median HR.

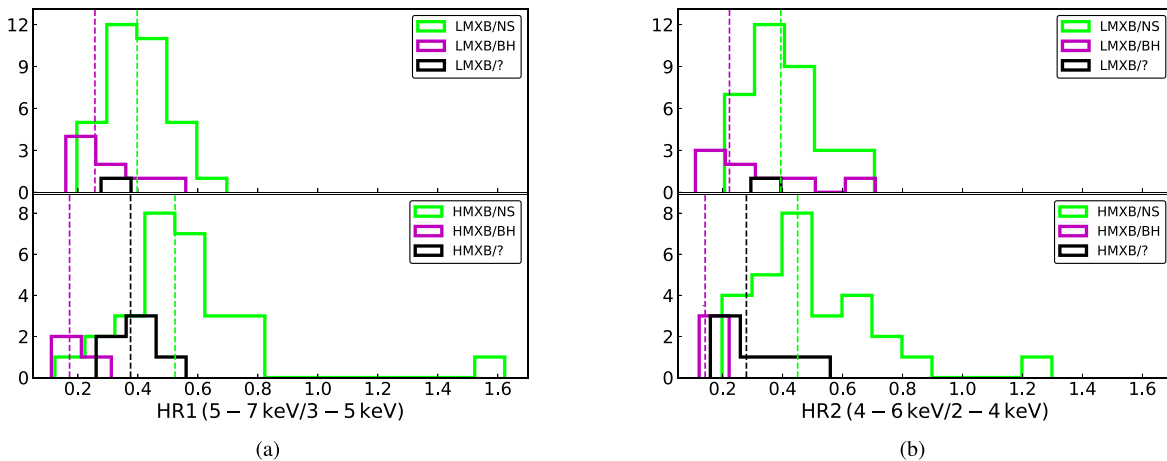


Figure 7. The histogram (bin size = 0.1) of HR distribution for the XRBs. The y-axis represents the source number, and the x-axis corresponds to HR. The dashed lines indicate the corresponding median HR.

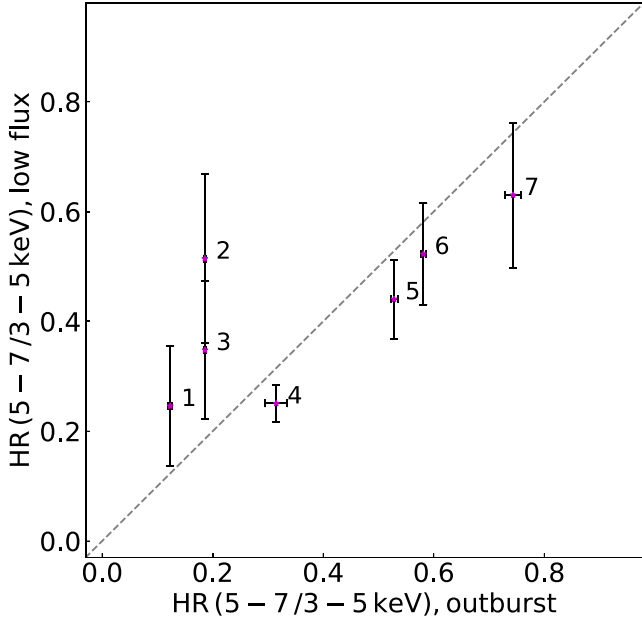


Figure 8. The relations between the averaged HR of seven XRBs during the outburst and low-flux processes. The x - and y -axes are the averaged HR during the two processes, respectively. GX 339–4, MAXI J1820+070, MAXI J1348+630, 4U 1722–30, GRS 1915+105, SWIFT J0243.6+6124, and 1A 0535+262 are labeled as # “1” to “7,” respectively.

assumed, and the results may not accurately reflect the real situations. Since our sample only contains one SNR, it is excluded and the domain is focused on the XRBs. The HR histograms for 7–40 keV/2–6 keV and 25–100 keV/2–6 keV are presented in Figure 9. The analysis of Table 7 and Figure 9 reveals that the spectra of NS HMXBs are consistently overall harder than those of NS LMXBs.

It can be seen that the spectra of the four BH systems vary from soft to hard, which is mainly related to the observation period. Different spectra can be observed at different times. Take the transient source MAXI J1348–630 as an example. During its quiescent state period, the X-ray radiation at 7–40 keV or 25–100 keV is undetectable by Insight-HXMT. Therefore, when calculating its HR, we can only use its fluxes from outburst. During the outburst, thermal emission likely from optically thin accretion disk and non-thermal processes (such as inverse-Compton scattering) from the corona are both present and dominate at different states (Carotenuto et al. 2021).

3.5. Spatial Distributions of Sources in the Three Variability Groups

A statistical analysis is conducted to determine the spatial distribution characteristics of F_v & S_v , F_s & S_s , and F_s & S_s sources across both galactic longitude (l) and galactic latitude (b). The

hard and soft bands as 4–6 and 2–4 keV are selected because the number of sources is the largest in this combination. The specific number can be found in Table 2, while the distribution histograms (including the distribution width of 68% sources) and sky maps are presented in Figures 10 and 11, respectively. Different colors are assigned to represent different variability groups.

During the monitoring period of Insight-HXMT, the majority of sources exhibit variable flux, while some have stable energy spectra. Additionally, more than half of the sources display spectral variability. Roughly one-third are flux-stable. Their distributions show varying aggregation trends, as seen in Figures 10 and 11.

1. The distribution of F_v & S_s sources appears to be more uniform compared to the other two variability groups.
2. The F_v & S_v sources exhibit a significant clustering trend, with over 90% being within $|l| < 45^\circ$. Moreover, 68% are concentrated in the region $-25^\circ < l < 9^\circ$. While their overall latitudinal distribution appears to be widespread, 68% are concentrated between -1.3° and 1.4° .
3. The F_s & S_s sources exhibit an extremely obvious clustering trend, with 68% concentrating within a small range of l from 19° to 42° and a narrow interval of b between -0.9° and 0.6° .

Each variability group exhibits a different spatial distribution in both l and b . The mechanism behind the distributions is not yet clear, while it is a very meaningful topic. A comprehensive analysis of the underlying reasons is beyond the scope of this article, further studies need to be conducted in the future.

3.6. Possible Relation between HR and Spatial Distributions

In this section, we investigate the possible relationships between their HR and spatial distributions. Bright sources are selected based on varying l and b , with differences in l (or b) ignored when exploring the relationships between HR and b (or l). Furthermore, different steps of b (or l) are selected to ensure that each region has the same number of sources, and the averaged HR in each region is used to represent the overall HR situation. Figure 12 illustrates the relationships between the HR and spatial distributions of all sources. Panel (a) shows that the HR in the region of $|l| < 20^\circ$ are generally larger than those at $|l| > 20^\circ$, regardless of which energy band of the hard band is selected. This phenomenon becomes less significant as the energy of the soft band becomes higher (panels (c) and (e)). We speculate that this phenomenon is due to the absorption of low-energy X-ray photons (especially below 2 keV) in the galactic center. In the right-hand panels, the overall fluctuation range of HR gradually narrows as the energy of the soft band increases, which may also be affected by absorption of the Galactic medium at a low energy band.

Table 6
The Information of Seven Transient XRBs

Number	Source Name	R.A. (deg)	Decl. (deg)	Source Type	HR (Outburst) 5–7/3–5 keV	HR (Low Flux) 5–7/3–5 keV
1	GX 339–4	255.71	–48.79	(BH)HMXB	0.123 ± 0.004	0.25 ± 0.11
2	MAXI J1820+070	275.09	7.19	(BH)LMXB	0.186 ± 0.002	0.51 ± 0.15
3	MAXI J1348–630	207.05	–63.27	(BH)LMXB	0.186 ± 0.002	0.35 ± 0.13
4	4U 1722–30	261.89	–30.8	(NS)LMXB	0.32 ± 0.02	0.25 ± 0.03
5	GRS 1915+105	288.80	10.95	(BH)LMXB	0.530 ± 0.006	0.46 ± 0.07
6	SWIFT J0243.6+6124	40.92	61.43	(NS)HMXB	0.581 ± 0.004	0.52 ± 0.09
7	1A 0535+262	84.73	26.32	(NS)HMXB	0.74 ± 0.01	0.6 ± 0.1

Table 7
The Fitted Spectral Information of the 31 Bright Sources

Source Name	Source Type	N_{H} $\times 10^{21}(\text{cm}^2)$	Photon Index (Γ)	Normalization ($\text{photon cm}^{-2} \text{s}^{-1} \text{keV}^{-1}$)	S Variability 7–40/2–6	S Variability 25–100/2–6
Crab ^a	SNR	3.6	2.11	8.76	S	S
GX 349+2	(NS)LMXB	4.65	2.8 ± 0.4	13 ± 8	V	V
GX 354-0	(NS)LMXB	12.9	2.2 ± 0.1	0.7 ± 0.2	V	V
GX 5-1	(NS)LMXB	8.07	2.8 ± 0.4	17 ± 9	V	V
GX 9+1	(NS)LMXB	8.29	2.9 ± 0.4	14 ± 8	V	V
GX 17+2	(NS)LMXB	8.52	2.8 ± 0.4	11 ± 7	V	V
H 1820-303	(NS)LMXB	1.33	2.8 ± 0.5	5 ± 3	V	V
4U 1722-30	(NS)LMXB	5.59	2.29 ± 0.05	0.14 ± 0.01	S	V
4U 1812-12	(NS)LMXB	6.29	1.86 ± 0.04	0.047 ± 0.005	S	S
Ser X-1	(NS)LMXB	4.38	3.0 ± 0.3	6 ± 2	V	S
H 1608-522	(NS)LMXB	16.6	2.28 ± 0.02	0.37 ± 0.01	V	V
H 1636-536	(NS)LMXB	3.02	2.05 ± 0.03	0.3 ± 0.02	V	V
GX 340+0	(NS)LMXB	21.6	2.7 ± 0.5	6 ± 5	V	V
4U 1735-444	(NS)LMXB	2.73	2.7 ± 0.4	2 ± 1	V	S
H 1702-429	(NS)LMXB	10.0	2.05 ± 0.03	0.29 ± 0.03	V	V
3A 1822-371	(NS)LMXB	1.03	1.75 ± 0.05	0.051 ± 0.009	V	V
H 0614+091	(NS)LMXB	4.63	2.53 ± 0.03	0.6 ± 0.03	V	V
GRS 1915+105	(BH)LMXB	13.9	1.7 ± 0.3	0.1 ± 0.1	V	V
GRS 1758-258	(BH)LMXB	6.0	1.7 ± 0.2	0.1 ± 0.1	V	V
MAXI J1348-630	(BH)LMXB	14.9	1.19 ± 0.03	0.11 ± 0.01	V	V
4U 1700-377	(NS)HMXB	5.19	1.5 ± 0.3	0.1 ± 0.2	V	V
H 1417-624	(NS)HMXB	11.2	1.6 ± 0.2	0.07 ± 0.05	V	V
H 1538-522	(NS)HMXB	7.38	1.9 ± 0.2	0.08 ± 0.04	V	V
Cen X-3	(NS)HMXB	11.0	2.1 ± 0.5	0.6 ± 0.6	V	V
GX 301-2	(NS)HMXB	14.2	1.3 ± 0.3	0.06 ± 0.07	V	V
Cyg X-3	(NS)HMXB	11.8	1.93 ± 0.07	0.48 ± 0.09	V	V
SWIFT J0243.6+6124	(NS)HMXB	7.26	1.5 ± 0.2	0.7 ± 0.4	V	V
1A 0535+262	(NS)HMXB	4.39	1.3 ± 0.01	0.043 ± 0.002	V	V
Vela X-1	(NS)HMXB	3.65	1.5 ± 0.2	0.13 ± 0.08	V	V
GRO J1008-57	(NS)HMXB	12.2	1.7 ± 0.3	0.06 ± 0.05	V	V
Cyg X-1	(BH)HMXB	7.05	2.37 ± 0.1	9 ± 1	V	V

Notes. The long-term HR variability of the 31 sources in the 7–40/2–6 keV and 25–100/2–6 keV are listed in the last two columns. “S” indicates that the HR is stable over time, while “V” indicates that the HR is variable.

^a Crab is used as the calibration for PSF, and its Γ and N_0 are listed.

4. Summary

Statistical analyses on the HR of the bright sources in the 4 yr GPSS catalog of Insight-HXMT are conducted. The sources are divided into three variability groups, including

$F_v \& S_v$, $F_v \& S_s$, and $F_s \& S_s$. We analyze the distribution characteristics of the HR for different types of sources in the three groups, including XRBs in different combinations of hard and soft bands, different types of bright sources at energy bands

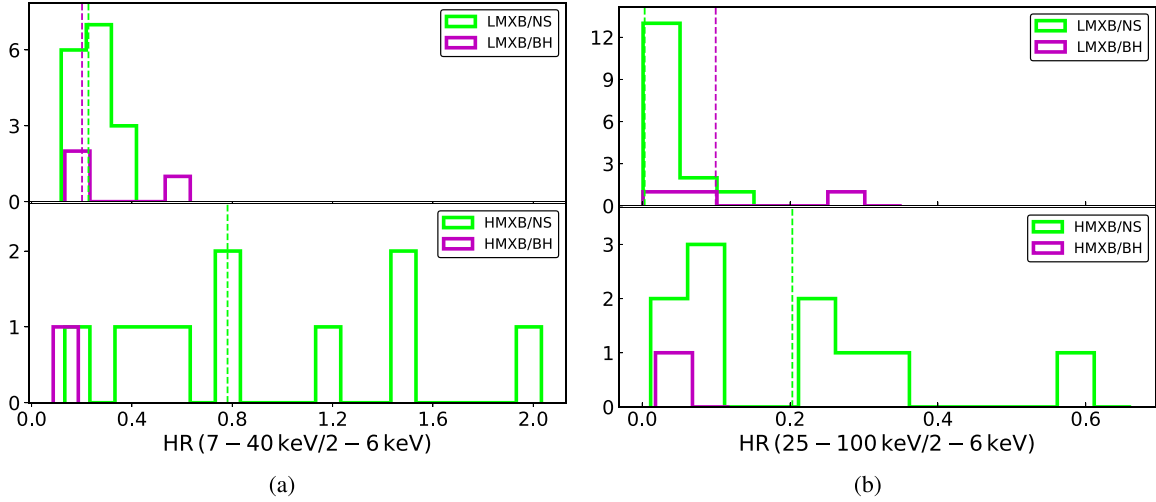


Figure 9. The histogram of HR distributions of the 30 bright XRBs. The dashed lines in each sub-panel indicate the corresponding median HR. The bin size in panels (a) and (b) are 0.1 and 0.05, respectively.

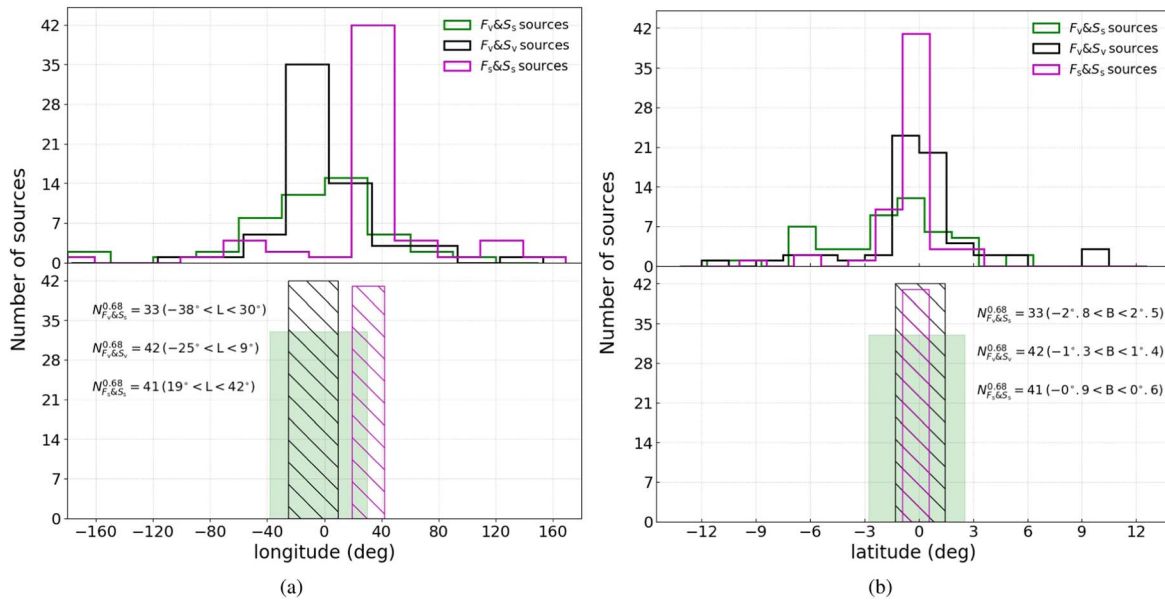


Figure 10. (Top cap) The bright source distributions for three variability groups as a function of l and b along the galactic plane, with different colors assigned to each variability group. (Bottom cap) The distribution width of 68% of the sources. The width of the three colored columns indicates the distribution width along l or b , while the height corresponds to the number of sources.

below 7 keV, and bright sources detected at 2–6, 7–40, and 25–100 keV. Additionally, the spatial distribution characteristics of the sources and HR are studied.

As the XRBs constitute a significant proportion of our catalog, their HRs are analyzed first. Our analysis revealed that most XRBs exhibit flux variability. Additionally, the energy spectra of HMXBs are consistently harder than those of LMXBs, which is consistent with previous studies Fabbiano (2006). It is worth noting that F_v & S_v LMXBs tend to be harder

than F_v & S_s LMXBs, while the opposite is true for HMXBs (below 7 keV). This discrepancy is primarily due to differences in radiation mechanisms.

The majority of X-ray flux from our brightest sources is found below 7 keV. The bright sources detected by LE are analyzed to identify the potential types of the unclassified sources through their HR of 4–6 keV/2–4 keV and 5–7 keV/3–5 keV, respectively. Our analyses suggest that LMXBs may be responsible for a larger proportion of unclassified sources

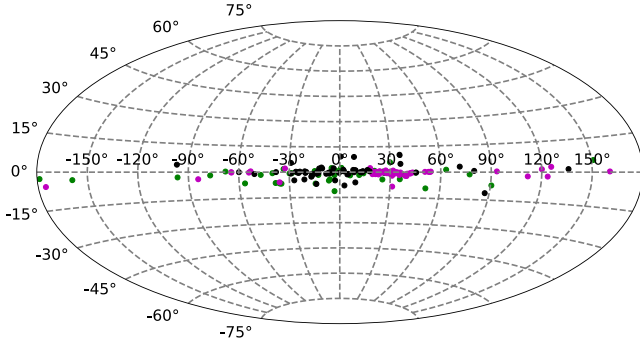


Figure 11. Aitoff projection shows the distribution of sources with different variabilities. Colors are the same as that in Figure 10.

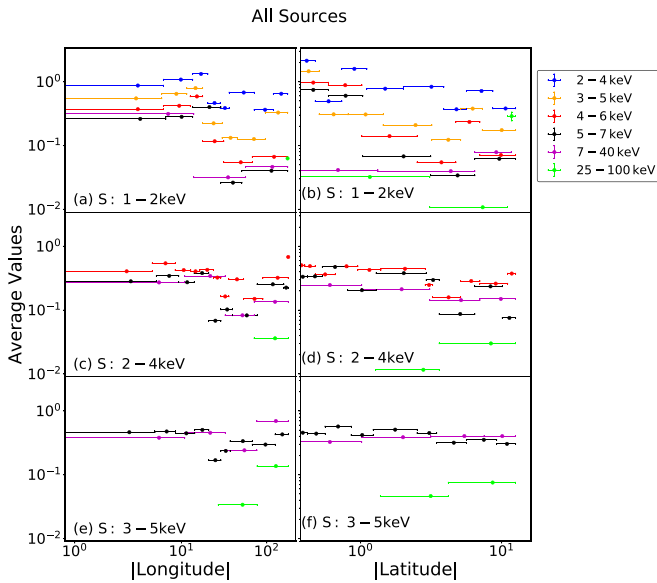


Figure 12. The relations between the averaged HR and spatial distributions. The Y-axes are the average values of HR of all sources at different regions, while the X-axes of the left and right panels are the absolute values of l and b , respectively. Panels from top to bottom are plotted for different soft bands: 1–2, 2–4, and 3–5 keV. The hard bands are represented by different colors. The horizontal and vertical error bars represent spatial steps and HR statistical error, respectively.

than others. Furthermore, for XRBs with ambiguous compact stars, the NS binaries are likely to be dominant. It is found that the X-ray spectral hardness of NS HMXBs, NS LMXBs and BH systems decreases in sequential order. This can be mainly attributed to two factors: first, whether the intrinsic magnetic field strength is sufficient to drag the gas fed by the companion toward the magnetic pole or form an accretion disk, and second, whether the primary star has a solid surface. These

factors contribute to the different X-ray radiation originating from various regions, such as the accretion column at the magnetic pole, the accretion disk, or the surface of the primary star, resulting in distinct shapes of the energy spectrum.

Seven XRBs are observed in their outbursts during the first 4 yr GPSS. The averaged HR of 4U 1722–30, GRS 1915 +105, SWIFT J0243.6+6124, and 1A 0535+262 shows consistency between their low-flux and outburst states. In addition, the HR of the two NS HMXBs is larger than that of the five LMXBs and BH binaries.

As the energy band increases, the radiation emitted by majority of X-ray sources tends to decrease. Thus, 31 sources (18 LMXBs, 12 HMXBs and one SNR) are left by constraining the sources with a flux S/N greater than 5 at 2–6, 7–40 and 25–100 keV, and an HR S/N at least 3. We analyze their HR of 25–100 keV/2–6 keV and 7–40 keV/2–6 keV, and make the assumption that the energy spectrum of each source is a power law. The analysis reveals that the spectra of NS HMXBs are generally harder than those of NS LMXBs, which further supports the conclusion in Sections 3.1 and 3.2.

The spatial distributions of F_v & S_v , F_v & S_s , and F_s & S_s sources display distinct patterns. The F_v & S_s sources are scattered across the galactic plane, whereas 68% of the F_v & S_v sources concentrate in the region of $-20^\circ < l < 9^\circ$. The F_s & S_s sources tend to cluster in $19^\circ < l < 42^\circ$, and mainly concentrate in the narrow region of $|b| < 0^\circ.9$.

Finally, the absorption of soft X-rays in the Galactic Plane can be reflected in the relation between the HR and its spatial distributions.

Acknowledgments

This work made use of the data from the Insight-HXMT mission, a project funded by the China National Space Administration (CNSA) and the Chinese Academy of Sciences (CAS). The authors are thankful for the support from the National Natural Science Foundation of China under grant Nos. 12333007, U1838202, U1838201, U1838107, U1838113, U1838113 and U2038102, the Youth Innovation Promotion Association of the CAS (grant id 2018014), and the National Key R&D Program of China (grant No. 2021YFA0718500). This work was partially supported by the International Partnership Program of the Chinese Academy of Sciences (grant No. 113111KYSB20190020).

Appendix A

The Table on the Data used in this Work

A portion of statistical analysis data for this article.

Table A1
Information of LMXBs at 2–4 keV and 4–6 keV

Name	Type	R.A. (deg)	Decl. (deg)	HR 4–6 keV/2–4 keV	DoF	χ^2	χ^2_{limit}	HR _{var}	F_{rms} 2–4 keV	F_{var} 2–4 keV	F_{rms} 4–6 keV	F_{var} 4–6 keV
GX 349+2	LMXB/NS	256.43	−36.42	0.497 ± 0.002	111	1025.2	110.3	V	0.0207 ± 0.001	V	0.062 ± 0.002	V
IGR J17091−3624	LMXB/BH	257.28	−36.41	0.45 ± 0.02	15	25.8	14.3	V	34 ± 1	V	41 ± 2	V
4U 1722−30	LMXB/NS	261.89	−30.80	0.28 ± 0.01	128	182.6	127.3	V	4.4 ± 0.3	V	3.2 ± 0.5	V
3A 1728−169	LMXB/NS	262.93	−16.96	0.394 ± 0.002	125	195.6	124.3	V	0.0078 ± 0.0008	V	0.01 ± 0.002	V
GX 354−0	LMXB/NS	262.99	−33.83	0.469 ± 0.009	65	229.7	64.3	V	0.43 ± 0.02	V	0.48 ± 0.03	V
1A 1742−294	LMXB/NS	266.52	−29.51	0.23 ± 0.04	2	35.4	1.4	V	2.3 ± 0.4	V	2.6 ± 0.5	V
GX 3+1	LMXB/NS	266.98	−26.56	0.41 ± 0.03	5	10.6	4.4	V	0.05 ± 0.01	V	0.1 ± 0.02	V
1H 1746−370	LMXB/NS	267.55	−37.05	0.34 ± 0.01	132	94.7	131.3	S	0.42 ± 0.06	V	0.3 ± 0.1	V
GX 5−1	LMXB/NS	270.28	−25.08	0.558 ± 0.001	121	2805.6	120.3	V	0.0255 ± 0.0009	V	0.034 ± 0.001	V
GX 9+1	LMXB/NS	270.39	−20.53	0.536 ± 0.002	99	823.9	98.3	V	0.031 ± 0.002	V	0.023 ± 0.002	V
XTE J1806−246	LMXB/NS	271.71	−24.58	0.41 ± 0.02	115	114.0	114.3	S	10.4 ± 0.5	V	18 ± 1	V
GX 13+1	LMXB/NS	273.63	−17.16	0.43 ± 0.004	67	2982.7	66.3	V	0.079 ± 0.004	V	0.064 ± 0.004	V
GX 17+2	LMXB/NS	274.01	−14.04	0.538 ± 0.001	194	640.1	193.3	V	0.0108 ± 0.0005	V	0.0207 ± 0.0008	V
H 1820−303	LMXB/NS	275.92	−30.36	0.418 ± 0.001	149	480.6	148.3	V	0.042 ± 0.001	V	0.07 ± 0.003	V
Ginga 1826−24	LMXB/NS	277.37	−23.80	0.337 ± 0.001	191	811.3	190.3	V	0.032 ± 0.001	V	0.074 ± 0.004	V
4U 1730−335	LMXB/NS	263.35	−33.39	0.44 ± 0.02	26	78.9	25.3	V	1.5 ± 0.1	V	2.6 ± 0.2	V
XB 1732−304	LMXB/NS	263.95	−30.48	0.1 ± 0.03	34	26.0	33.3	S	1 ± 1	V	<0	S
SLX 1735−269	LMXB/NS	264.57	−26.99	0.25 ± 0.04	23	18.2	22.3	S	1.4 ± 0.4	V	0 ± 1	S
SWIFT J174510.8−2624	LMXB/BH	266.29	−26.40	0.47 ± 0.05	11	11.9	10.3	V	2.8 ± 0.3	V	1.5 ± 0.2	V
1A 1744−361	LMXB/NS	267.08	−36.12	0.23 ± 0.05	65	18.5	64.3	S	4 ± 2	V	<0	S
H 1755−338	LMXB/BH	269.67	−33.81	0.213 ± 0.006	83	88.8	82.3	V	12.8 ± 0.4	V	3.5 ± 0.5	V
GRS 1758−258	LMXB/BH	270.30	−25.74	0.19 ± 0.03	39	79.9	38.3	V	51 ± 1	V	13.8 ± 0.9	V
4U 1812−12	LMXB/NS	273.78	−12.10	0.23 ± 0.02	102	76.4	101.3	S	0.1 ± 0.1	S	<0	S
EXO 1846−031	LMXB/BH	282.32	−3.06	0.25 ± 0.01	53	16.0	52.3	S	157 ± 2	V	36 ± 1	V
3A 1850−087	LMXB/NS	283.27	−8.71	0.2 ± 0.03	120	30.8	119.3	S	0.5 ± 0.2	V	<0	S
4U 1916−053	LMXB/NS	289.70	−5.24	0.32 ± 0.04	81	17.6	80.3	S	0.2 ± 0.2	S	<0	S
SAX J1828.5−1037	LMXB/NS	277.14	−10.62	0.25 ± 0.04	54	25.4	53.3	S	0.6 ± 0.4	V	<0	S
Ser X−1	LMXB/NS	279.99	5.04	0.38 ± 0.001	127	316.6	126.3	V	0.0138 ± 0.0009	V	0.022 ± 0.002	V
4U 1957+115	LMXB/BH	299.85	11.71	0.325 ± 0.006	51	37.3	50.3	S	0.075 ± 0.009	V	0.08 ± 0.02	V
4U 1543−624	LMXB/NS	236.98	−62.57	0.27 ± 0.03	50	12.5	49.3	S	0.6 ± 0.2	V	<0	S
H 1608−522	LMXB/NS	243.18	−52.42	0.336 ± 0.004	90	148.2	89.3	V	43.3 ± 0.7	V	36.7 ± 0.7	V
H 1636−536	LMXB/NS	250.23	−53.75	0.352 ± 0.006	128	177.2	127.3	V	0.45 ± 0.02	V	0.3 ± 0.04	V
GX 340+0	LMXB/NS	251.45	−45.61	0.7 ± 0.006	33	890.7	32.3	V	0.025 ± 0.003	V	0.018 ± 0.002	V
1H 1556−605	LMXB/NS	240.26	−60.74	0.4 ± 0.1	28	5.6	27.3	S	<0	S	<0	S
MAXI J1348−630	LMXB/BH	207.05	−63.27	0.151 ± 0.001	53	657.1	52.3	V	6449 ± 12	V	714 ± 5	V
H 1624−490	LMXB/NS	247.01	−49.20	0.7 ± 0.03	44	71.1	43.3	V	0.48 ± 0.06	V	0.35 ± 0.04	V
H 1705−440	LMXB/NS	257.23	−44.10	0.481 ± 0.003	88	1234.2	87.3	V	0.61 ± 0.01	V	0.71 ± 0.02	V
4U 1735−444	LMXB/NS	264.74	−44.45	0.405 ± 0.003	119	501.2	118.3	V	0.081 ± 0.003	V	0.141 ± 0.007	V
XTE J1701−407	LMXB/NS	255.43	−40.86	0.39 ± 0.06	26	11.9	25.3	S	1.6 ± 0.5	V	1.8 ± 0.6	V
H 1702−429	LMXB/NS	256.56	−43.04	0.37 ± 0.01	72	310.8	71.3	V	0.6 ± 0.04	V	1.04 ± 0.09	V
4U 1708−40	LMXB/NS	258.10	−40.84	0.23 ± 0.02	72	155.3	71.3	V	1.2 ± 0.2	V	0.9 ± 0.3	V
3A 1822−371	LMXB/NS	276.45	−37.10	0.67 ± 0.03	79	32.1	78.3	S	0.12 ± 0.08	V	<0	S
H 1822−000	LMXB/?	276.34	−0.01	0.33 ± 0.01	119	56.7	118.3	S	0.05 ± 0.03	V	<0	S
Aql X−1	LMXB/NS	287.82	0.58	0.347 ± 0.004	51	44.0	50.3	S	468 ± 3	V	315 ± 5	V
MAXI J1820+070	LMXB/BH	275.09	7.19	0.1215 ± 0.001	27	4983.6	26.3	V	1378 ± 4	V	110 ± 1	V
4U 1323−62	LMXB/NS	201.65	−62.14	0.27 ± 0.07	61	10.7	60.3	S	<0	S	<0	S
Cyg X−2	LMXB/NS	326.17	38.32	0.375 ± 0.002	28	94.2	27.3	V	0.149 ± 0.005	V	0.167 ± 0.008	V
H 0614+091	LMXB/NS	94.28	9.14	0.301 ± 0.006	62	53.1	61.3	S	0.22 ± 0.02	V	0.29 ± 0.04	V
1H 1254−690	LMXB/NS	194.40	−69.29	0.34 ± 0.01	65	44.0	64.3	S	0.06 ± 0.02	V	<0	S
GRS 1915+105	LMXB/BH	288.80	10.95	0.664 ± 0.006	50	192.4	49.3	V	261 ± 1	V	467 ± 2	V

Table A2
Information of HMXBs at 2–4 keV and 4–6 keV

Name	Type	R.A. (deg)	Decl. (deg)	HR 4–6 keV/2–4 keV	DoF	χ^2	χ^2_{limit}	HR _{var}	F_{rms} 2–4 keV	F_{var} 2–4 keV	F_{rms} 4–6 keV	F_{var} 4–6 keV
IGR J18027–2016	HMXB/NS	270.67	–20.29	0.45 ± 0.01	13	108.1	12.3	V	12.1 ± 0.6	V	14.3 ± 0.7	V
SAX J1818.6–1703	HMXB/NS	274.66	–17.05	0.22 ± 0.03	57	55.6	56.3	S	5.3 ± 0.6	V	8 ± 1	V
4U 1700–377	HMXB/NS	255.99	–37.84	0.79 ± 0.03	93	185.1	92.3	V	16 ± 1	V	8.9 ± 0.4	V
GRO J1750–27	HMXB/NS	267.30	–26.65	0.35 ± 0.02	5	82.7	4.4	V	1.12 ± 0.08	V	5.2 ± 0.4	V
IGR J17586–2129	HMXB/?	269.64	–21.39	0.36 ± 0.03	58	65.4	57.3	V	196 ± 7	V	89 ± 4	V
IGR J18214–1318	HMXB/NS	275.33	–13.31	0.24 ± 0.03	58	68.7	57.3	V	26 ± 2	V	1.9 ± 0.8	V
IGR J18256–1035	HMXB/?	276.43	–10.58	0.18 ± 0.05	59	9.7	58.3	S	1.0 ± 0.9	V	<0	S
IGR J18483–0311	HMXB/NS	282.07	–3.17	0.4 ± 0.06	43	10.4	42.3	S	9 ± 1	V	<0	S
XTE J1855–026	HMXB/NS	283.88	–2.61	0.28 ± 0.05	89	20.5	88.3	S	0.2 ± 0.8	S	<0	S
Ginga 1839–04	HMXB/?	280.45	–4.50	0.25 ± 0.05	64	10.6	63.3	S	<0	S	>0	S
IGR J18450–0435	HMXB/NS	281.26	–4.57	0.27 ± 0.06	50	10.0	49.3	S	<0	S	>0	S
4U 1901+03	HMXB/NS	285.90	3.19	0.55 ± 0.04	72	41.4	71.3	S	7 ± 1	V	12 ± 2	V
H 1417–624	HMXB/NS	215.30	–62.70	0.36 ± 0.05	45	35.8	44.3	S	0.5 ± 0.3	V	0.2 ± 0.2	V
Cir X–1	HMXB/NS	230.17	–57.17	0.487 ± 0.002	129	1409.2	128.3	V	5.29 ± 0.04	V	4.91 ± 0.05	V
IGR J16465–4507	HMXB/NS	251.65	–45.12	0.39 ± 0.04	13	97.8	12.3	V	4.8 ± 0.4	V	18 ± 1	V
GX 339–4	HMXB/BH	255.71	–48.79	0.135 ± 0.002	73	1359.3	72.3	V	129.0 ± 0.9	V	30.3 ± 0.9	V
IGR J16283–4838	HMXB/?	247.04	–48.65	0.48 ± 0.04	25	35.4	24.3	V	0.9 ± 0.1	V	1.7 ± 0.3	V
IGR J16318–4848	HMXB/NS	247.95	–48.82	0.5 ± 0.06	10	28.0	9.3	V	1.5 ± 0.4	V	1.3 ± 0.5	V
IGR J16418–4532	HMXB/NS	250.46	–45.54	0.42 ± 0.06	17	31.5	16.3	V	4.2 ± 0.4	V	9 ± 1	V
Ginga 1839–06	HMXB/?	280.42	–5.90	0.18 ± 0.04	67	17.7	66.3	S	0.9 ± 0.3	V	<0	S
AX J1835.4–0737	HMXB/NS	278.87	–7.62	0.32 ± 0.06	52	6.3	51.3	S	<0	S	<0	S
Sct X–1	HMXB/NS	279.12	–7.61	0.17 ± 0.05	76	10.6	75.3	S	<0	S	<0	S
H 1538–522	HMXB/NS	235.60	–52.39	0.44 ± 0.04	90	37.9	89.3	S	<0	S	<0	S
4U 1543–47	HMXB/BH	236.79	–47.67	0.1852 ± 0.0008	46	57.1	45.3	V	152 857 ± 201	V	15 525 ± 60	V
SS 433	HMXB/?	287.96	4.98	0.3 ± 0.04	89	28.6	88.3	S	<0	S	<0	S
4U 1909+07	HMXB/NS	287.70	7.60	0.41 ± 0.09	47	7.8	46.3	S	<0	S	<0	S
Cen X–3	HMXB/NS	170.32	–60.62	0.612 ± 0.009	64	38.3	63.3	S	9.2 ± 0.2	V	10.8 ± 0.3	V
1E 1145.1–6141	HMXB/NS	176.87	–61.95	0.42 ± 0.07	45	12.6	44.3	S	<0	S	<0	S
GX 301–2	HMXB/NS	186.66	–62.77	1.2 ± 0.08	79	100.9	78.3	V	0.7 ± 0.6	V	1.6 ± 0.2	V
IGR J19294+1816	HMXB/NS	292.48	18.31	0.39 ± 0.05	66	22.7	65.3	S	<0	S	<0	S
XTE J1946+274	HMXB/NS	296.41	27.36	0.66 ± 0.06	44	13.2	43.3	S	1 ± 1	V	<0	S
EXO 2030+375	HMXB/NS	308.06	37.64	0.48 ± 0.05	52	32.5	51.3	S	10 ± 1	V	5 ± 1	V
Cyg X–3	HMXB/NS	308.11	40.96	0.713 ± 0.004	77	689.0	76.3	V	2.32 ± 0.04	V	2.29 ± 0.04	V
Cyg X–1	HMXB/BH	299.59	35.20	0.1417 ± 0.0003	146	17 808.6	145.3	V	0.137 ± 0.001	V	0.271 ± 0.004	V
3A 0114+650	HMXB/NS	19.51	65.29	0.67 ± 0.09	64	8.0	63.3	S	<0	S	<0	S
SWIFT J0243.6+6124	HMXB/NS	40.92	61.43	0.504 ± 0.003	61	107.5	60.3	V	5141 ± 12	V	2816 ± 11	V
1A 0535+262	HMXB/NS	84.73	26.32	0.68 ± 0.01	48	31.8	47.3	S	132 ± 2	V	157 ± 3	V
Vela X–1	HMXB/NS	135.53	–40.56	0.83 ± 0.02	59	169.2	58.3	V	5.4 ± 0.2	V	2.03 ± 0.1	V
GRO J1008–57	HMXB/NS	152.44	–58.29	0.66 ± 0.04	45	17.7	44.3	S	9.2 ± 0.9	V	10 ± 1	V

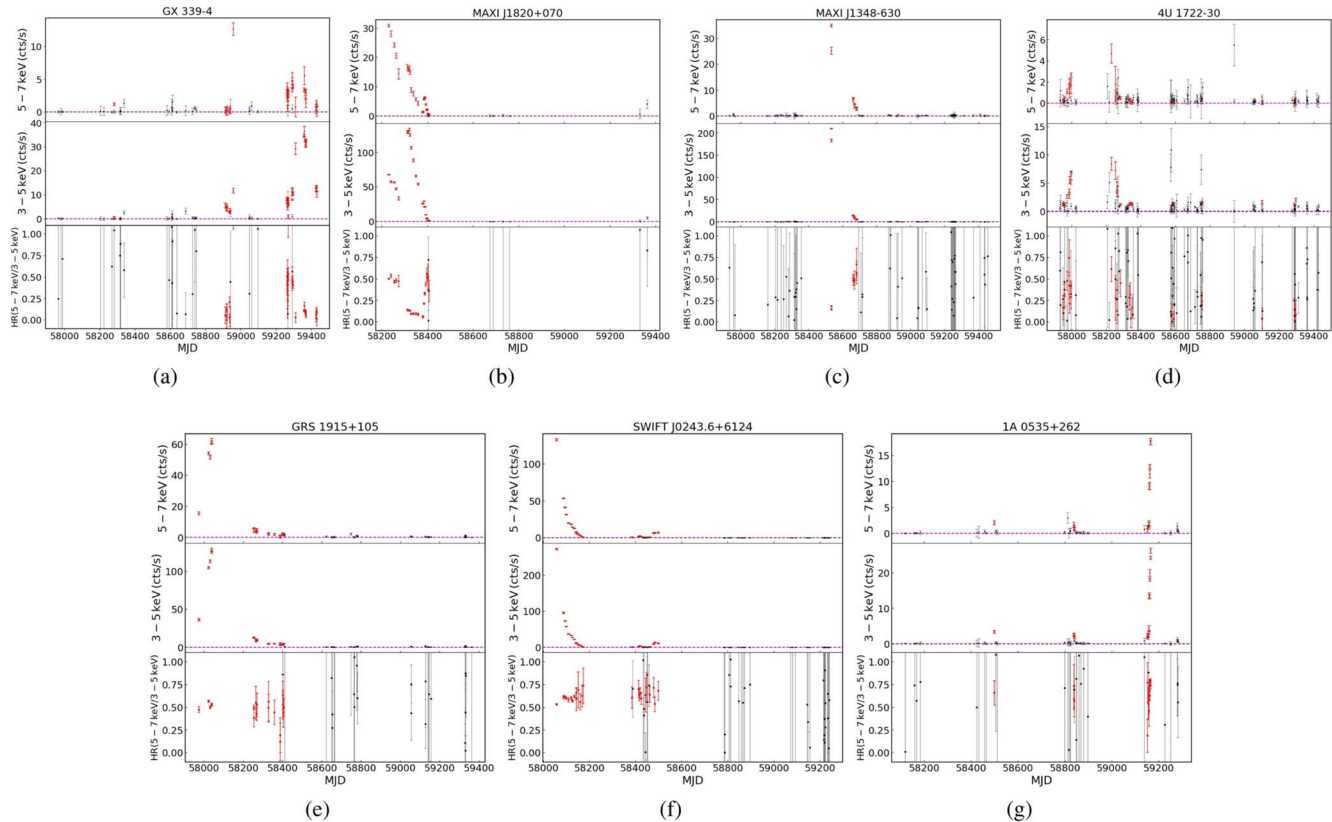


Figure B1. The long-term light curves and HR of seven transient XRBs with observed outbursts. The red and black points indicate the outburst and low-flux states, respectively.

Appendix B

The Long-term Light Curves and HR of Seven Transient XRBs with Observed Outbursts

This figure shows the long-term light curves and HR of seven transient XRBs, which have been observed outbursts.

ORCID iDs

Chen Wang <https://orcid.org/0000-0002-3206-5293>
 Jin-Yuan Liao <https://orcid.org/0000-0001-8277-6133>
 Cheng-Kui Li <https://orcid.org/0000-0001-5798-4491>
 Na Sai <https://orcid.org/0000-0001-8378-5904>
 Jing Jin <https://orcid.org/0000-0002-7085-6328>
 Shuang-Nan Zhang <https://orcid.org/0000-0001-5586-1017>

References

Alpar, M. A., Cheng, A. F., Ruderman, M. A., & Shaham, J. 1982, *Natur*, **300**, 728
 Bahramian, A., Heinke, C. O., Kennea, J. A., et al. 2021, *MNRAS*, **501**, 2790
 Becker, P. A., & Wolff, M. T. 2007, *ApJ*, **654**, 435
 Belczynski, K., & Ziolkowski, J. 2009, *ApJ*, **707**, 870
 Bildsten, L., Chakrabarty, D., Chiu, J., et al. 1997, *ApJS*, **113**, 367
 Boller, T., Freyberg, M. J., Trümper, J., et al. 2016, *A&A*, **588**, A103
 Carotenuto, F., Corbel, S., Tremou, E., et al. 2021, *MNRAS*, **504**, 444
 Cusumano, G., La Parola, V., Segreto, A., et al. 2010, *A&A*, **524**, A64

Fabbiano, G. 2006, *ARA&A*, **44**, 323
 Homan, J., & Belloni, T. 2005, *Ap&SS*, **300**, 107
 Hong, J., Mori, K., Hailey, C. J., et al. 2016, *ApJ*, **825**, 132
 Hori, T., Shidatsu, M., Ueda, Y., et al. 2018, *ApJS*, **235**, 7
 Hoshi, R. 1984, *PASJ*, **36**, 785
 Jin, Y. K., Zhang, S. N., & Wu, J. F. 2006, *ApJ*, **653**, 1566
 Kawamuro, T., Ueda, Y., Shidatsu, M., et al. 2018, *ApJS*, **238**, 32
 Krivonos, R., Tsygankov, S., Lutovinov, A., et al. 2015, *MNRAS*, **448**, 3766
 Lamb, F. K., & Bouloukos, S. 2008, in *Astrophysics and Space Science Library*, ed. E. F. Milone, D. A. Leahy, & D. W. Hobill, Vol. 352 (Berlin: Springer), 87
 Madsen, K. K., Harrison, F. A., Markwardt, C. B., et al. 2015, *ApJS*, **220**, 8
 McClintock, J. E., & Remillard, R. A. 2006, *Compact Stellar X-ray Sources*, Vol. 39, 157
 Mitsuda, K., Inoue, H., Koyama, K., et al. 1984, *PASJ*, **36**, 741
 Mukai, K. 2017, *PASP*, **129**, 062001
 Nang, Y., Liao, J.-Y., Sai, N., et al. 2020, *JHEAp*, **25**, 39
 Poutanen, J. 2006, *AdSpR*, **38**, 2697
 Psaltis, D. 2004, arXiv:astro-ph/0410536
 Reig, P. 2011, *Ap&SS*, **332**, 1
 Remillard, R. A., & McClintock, J. E. 2006, *ARA&A*, **44**, 49
 Russell, D. M., & Fender, R. P. 2008, *MNRAS*, **387**, 713
 Sai, N., Liao, J.-Y., Li, C.-K., et al. 2020, *JHEAp*, **26**, 1
 Saxton, R. D., Read, A. M., Esquej, P., et al. 2008, *A&A*, **480**, 611
 Sugizaki, M., Mihara, T., Serino, M., et al. 2011, *PASJ*, **63**, S635
 Vaughan, S., Edelson, R., Warwick, R. S., & Uttley, P. 2003, *MNRAS*, **345**, 1271
 Voges, W., Aschenbach, B., Boller, T., et al. 1999, *A&A*, **349**, 389
 Wang, C., Liao, J.-Y., Guan, J., et al. 2023, *ApJS*, **265**, 52
 Wani, K. A., & Gaur, H. 2020, *Galax*, **8**, 59
 White, N. E., Swank, J. H., & Holt, S. S. 1983, *ApJ*, **270**, 711
 Zhang, S.-N. 2013, *FrPhy*, **8**, 630
 Zhang, S. N., Cui, W., Harmon, B. A., et al. 1997, *ApJL*, **477**, L95
 Zhang, S.-N., Li, T., Lu, F., et al. 2020, *SCPMA*, **63**, 249502